Analytical derivation of phase-current waveform for elimination of torque and input-current ripples of switched reluctance motor operating under magnetic saturation

Takayuki Kusumi, Kosuke Kobayash, Kazuhiro Umetan, and Eiji Hiraki
Graduate school of natural science and technology,
Okayama University,
Okayama, Japan

Published in: IEEE Transactions on Industry Applications (Volume: 58, Issue: 4, July-Aug. 2022)

DOI: 10.1109/TIA.2022.3172898

Analytical Derivation of Phase-Current Waveform for Elimination of Torque and Input-Current Ripples of Switched Reluctance Motor Operating Under Magnetic Saturation

Takayuki Kusumi, *Member, IEEE*, Kosuke Kobayashi, *Non-member*, Kazuhiro Umetani and Eiji Hiraki, *Member, IEEE*

***Abstract*—Switched reluctance motors (SRMs) have recently attracted researchers' attention owing to their robust mechanical construction, high thermal tolerance, and strong cost-effectiveness, which are promising for vehicle propulsion. However, they tend to generate large ripples in the torque and input currents to the inverter; this deteriorates the driving comfort, and damages the battery lifetime. Preceding studies have investigated using the phase currents of SRMs to eliminate these ripples. However, these studies had difficulties in sufficiently eliminating these ripples in operations under magnetic saturation. This study further evolves one of these preceding studies, and proposes a derivation method for the phase-current waveform for improving the elimination of the torque and input-current ripples in operation under magnetic saturation. The proposed method analytically determines the phase-current waveform based on a nonlinear behavior model of the SRM while considering the magnetic saturation. A finite-element-method-based simulation and experiment are performed to evaluate the proposed method. These results reveal the successful reduction of the torque and input-current ripples under the magnetic saturation relative to a preceding study, supporting the appropriateness of the proposed method.**

***Index Terms*—Input-current ripple, magnetic saturation, phase-current waveform, switched reluctance motors, torque ripple.**

I. INTRODUCTION

ELECTRIC vehicles (EVs) have recently emerged and are becoming widespread as one of the most promising remedies for reducing fossil fuel consumption. Many of the commercially available EVs currently utilize an interior permanent magnet synchronous motor (IPMSM) as a propulsion motor. The IPMSM is known to have a high power density and to exhibit high efficiency over a wide range of torques and rotation speeds. However, the IPMSM contains permanent magnets, resulting in a low thermal tolerance and a complicated mechanical construction of the motor. Furthermore, the permanent magnets require significant amounts of rare-earth materials, making the IPMSM suffer from unstable material supplies and high costs. These drawbacks of the IPMSM may cause difficulty in the application of the EV systems to low-price vehicles, as such vehicles tend to have limited cooling environments and severe requirements for stable material supply and low manufacturing costs. Thus, these drawbacks hinder the further spread of EVs.

Adopting a reluctance motor for the propulsion of low-price vehicles (instead of the IPMSM) may be an effective approach to overcoming this difficulty. Reluctance motors contain no permanent magnet, and are therefore free from the aforementioned drawbacks. Certainly, many of the reluctance motors suffer from a relatively small torque/power density. However, the switched reluctance motor (SRM) has recently emerged as a promising motor with a large torque/power density, and has motivated a number of researchers to investigate applying the SRM for vehicle propulsion [1][2].

Despite the attractive features of the SRM, the SRM nevertheless generates large ripples in the torque and input currents to the inverter driving the motor. The torque ripple generates a noise vibration and deteriorates the driving comfort, whereas the input-current ripple damages the battery lifetime. Certainly, the input-current ripple can be decoupled by a DC link capacitor attached at the input of the inverter, particularly at a high rotation speed. However, the input-current ripple has a low frequency in low-speed operation, causing difficulty in decoupling the ripple using the DC link capacitor. Therefore, both the torque and input-current ripples are severe drawbacks, and should be solved for vehicle application.

A number of studies have been dedicated to the reduction of these two ripples in the SRM [3]–[40]. The SRM has abundant harmonics in the electrical angle dependence of the phase

Manuscript received March 5, 2021; revised January 11, 2022; accepted April 6, 2022. This article was presented in part at IEEE Energy Conversion Congress and Exposition (ECCE2019), Baltimore, MD, USA, October 2019 [38].

Takayuki Kusumi was with Graduate School of Natural Science and Technology, Okayama University, 3-1-1 Tsushimanaka, Kita-Ku, Okayama, Japan until March 2021. He is currently with Mazda Motor Corporation, Hiroshima, Japan, from April 2021. (e-mail: p75s6ovi@s.okayama-u.ac.jp)

Kosuke Kobayashi was with Graduate School of Natural Science and Technology, Okayama University, 3-1-1 Tsushimanaka, Kita-Ku, Okayama, Japan until March 2021. He is currently with Honda R&D Co., Ltd., Saitama, Japan, from April 2021. (e-mail: pn9p7rfd@s.okayama-u.ac.jp)

Kazuhiro Umetani and Eiji Hiraki are with the Graduate School of Natural Science and Technology, Okayama University, 3-1-1 Tsushimanaka, Kita-Ku, Okayama, Japan (e-mail: umetani@okayama-u.ac.jp; hiraki@okayama-u.ac.jp)

inductance, i.e., in the phase inductance profile, as well as the strong non-linearity caused by the magnetic saturation. Therefore, the reduction of these ripples should consider both the harmonics and the non-linearity.

Many preceding studies have focused only on the reduction of the torque ripples [3]–[30]. The simple approach is to consider the harmonics in the phase inductance profile while neglecting the magnetic saturation. For example, [3]–[5] optimized the phase-current waveforms based on the phase inductance profile below the magnetic saturation level. Furthermore, [6]–[8] optimized both the phase-current waveform and pole shape to reduce the torque ripple with the minimum copper loss. A more complicated approach is to consider the harmonics in both the phase inductance profile and the magnetic saturation. For example, [9]–[27] optimized phase-current waveforms while further considering the nonlinear relation between the torque and phase current. These studies can be classified into two major approaches: [9], [11], and [13]–[16] took the numerical approach, and determined the phase-current waveform using a numerical search based on a database of the relationships among the torque, phase-current, and electrical angle, as obtained using a finite-element method (FEM) analysis or an experimentally determined phase inductance profile; [10], [12], and [17]–[27] took the analytical approach, and determined the phase current waveform based on analytically derived requirement conditions for eliminating the torque ripple by using an analytical model of the output torque. Additionally, [28]–[30] optimized both the phase-current waveform and the pole shape to reduce the torque ripple with the minimum copper loss: [30] took a numerical approach based on the FEM analysis to numerically search for both the pole shape and phase-current waveform; [28][29] took a semi-analytical approach, in which the phase-current waveform was determined analytically, whereas the pole shape was numerically optimized based on the FEM analysis.

Meanwhile, other preceding studies have targeted only the input-current ripple. For example, [31]–[35] reduced the input-current ripple, considering the magnetic saturation; [31] and [32] optimized the phase-current waveforms; and [33]–[35] proposed the new inverter topology and corresponding control method for the SRM.

The aforementioned studies have targeted either the torque ripple or the input-current ripple. However, a few studies have investigated the simultaneous reduction of the torque and input-current ripples: [36] optimized the phase-current waveform; [37] optimized both the phase-current waveform and the rotor shape for the simultaneous reduction of these two ripples with the minimum copper loss. These studies have proven the successful reduction of both the torque and input-current ripples in their experiments. However, the application of these studies is limited to operation with a low output torque, because these studies did not consider magnetic saturation. In fact, [36] and [37] indicated that both the torque and input-current ripples increased in the large magnetization of the SRM. Consequently, the simultaneous reduction of the torque and input-current ripples considering the magnetic saturation remains a challenging issue.

The purpose of this study is to propose a derivation method for a phase-current waveform for the simultaneous reduction of these two ripples, considering the magnetic saturation. The proposed method is based on a preceding study [36], as the phase-current waveform of this study is derived by modifying the phase-current waveform derived by [36] to compensate for the effect of the magnetic saturation.

The proposed method derives the phase-current waveform through a theoretical analysis of the behavior model of an SRM including the effect of the magnetic saturation. This study adopted the analytical approach rather than the numerical calculation to search for the phase-current waveform. According to the preceding studies [36] [37], an infinitely large number of phase-current waveforms were found to eliminate both the torque and input-current ripples. Therefore, the analytical formulation may be convenient for systematically deriving various waveforms from the same SRM model rather than a numerical calculation, which determines one phase-current waveform after a massive number of trial-and-errors.

This paper is an updated version of a conference paper [38]. Based on the conference paper, this paper further incorporates a detailed description of the derivation process of the phase-current waveform. Additionally, this study evaluated the proposed method with an FEM-based simulation along with the experiment. In the simulation and experiment, the phase-current waveform of the proposed method was compared with two phase-current waveforms: one was the traditional square-shape phase-current waveform; the other was the phase-current waveform of the previous method [36].

This paper comprises six sections. Section I (above) presented an overview of preceding studies addressing the reduction of the torque and input-current ripples for SRMs. This section discussed the difficulties of these preceding studies, and described the approach of this study to overcoming these difficulties. Section II briefly reviews the preceding method [36]. Section III analytically derives the proposed method. Sections IV and V present the FEM-based simulation and experiment for the commercially available SRM, respectively, aiming to evaluate the reduction effect on the torque and input-current ripples from the proposed method. Finally, Section VI provides the conclusions.

II. Review of Previous Method

The preceding study [36] derived a phase-current waveform for eliminating the torque and input-current ripples for an arbitrary inductance profile without considering the magnetic saturation. The derivation method was based on the analytical formulation of the torque and input currents contributed by each phase of the motor. Hereafter, this section reviews the method using a three-phase concentrated-windings SRM, as shown in Fig. 1. The following discussion is focused on the phase U. However, the same discussion also stands for the other phases, owing to the symmetry among the phases.

In the concentrated-winding SRM, the total magnetic co-energy E'_{total} can be approximated as the sum of the co-energy

contributed by each phase while neglecting the magnetic coupling among the phases, as follows:

$$E'_{total}(\theta_E, i_U, i_V, i_W) = E'_U(\theta_E, i_U) + E'_V(\theta_E, i_V) + E'_W(\theta_E, i_W), \tag{1}$$

where E'_U, E'_V, and E'_W are the magnetic co-energy contributed by the phases U, V, and W, respectively. In addition, i_U, i_V, and i_W are the phase currents of phases U, V, and W, respectively; and θ_E is the electrical angle. Owing to the symmetry among the phases, E'_V and E'_W can be expressed as follows:

$$\begin{aligned} E'_V(\theta_E, i_V) &= E'_U(\theta_E + 4\pi/3, i_V), \\ E'_W(\theta_E, i_W) &= E'_U(\theta_E + 2\pi/3, i_W). \end{aligned} \tag{2}$$

The magnetic co-energy of each phase is proportional to the square of the phase current of the phase, because the magnetic saturation is not considered. Therefore, the magnetic co-energy of phase U has a form as follows:

$$E'_U(\theta_E, i_U) = K_2(\theta_E) i_U^2, \tag{3}$$

where $K_2(\theta_E)$ is a given coefficient of the SRM under consideration. This coefficient is closely related to the phase inductance, owing to the relation as follows:

$$L_U(\theta_E) = \frac{\partial^2}{\partial i_U^2} E'_U(\theta_E, i_U) = 2K_2(\theta_E), \tag{4}$$

where $L_U(\theta_E)$ is the inductance of the phase U.

The torque is the partial derivative of the total magnetic co-energy E'_{total} with respect to the mechanical angle [39]. Because of the linearity of the differential operator, the torque can be expressed as the sum of the torque contributed by each phase, similarly to E'_{total}. Hence, the torque τ is expressed as follows:

$$\tau(\theta_E, i_U, i_V, i_W) = \tau_U(\theta_E, i_U) + \tau_V(\theta_E, i_V) + \tau_W(\theta_E, i_W), \tag{5}$$

where τ_U, τ_V, and τ_W are the torque contributed by phases U, V, and W, respectively. The torque contributed by phase U, i.e., τ_U, can be formulated as follows:

$$\tau_U(\theta_E, i_U) = \frac{\partial E'_U(\theta_E, i_U)}{\partial \theta_M} = P_r \frac{\partial E'_U(\theta_E, i_U)}{\partial \theta_E} = P_r \frac{\partial K_2(\theta_E)}{\partial \theta_E} i_U^2, \tag{6}$$

where θ_M is the mechanical angle, and P_r is the number of rotor poles.

Meanwhile, the DC input current to the inverter equals the sum of the electric power supplied to each phase of the SRM divided by the DC bus voltage V_{DC}, if the power loss at the inverter is neglected and the high-frequency ripples caused by the switching are eliminated from the input current. Therefore, the input current can also be expressed as follows:

$$i_E = \frac{i_U v_U}{V_{DC}} + \frac{i_V v_V}{V_{DC}} + \frac{i_W v_W}{V_{DC}} = i_{EU} + i_{EV} + i_{EW}, \tag{7}$$

where v_U, v_V, and v_W are the voltages applied to the phase windings of phases U, V, and W, respectively; i_{EU}, i_{EV}, and i_{EW} are the input currents contributed by phases U, V, and W, respectively. The high-frequency ripples from the switching are assumed to be eliminated from v_U, v_V, and v_W. Equation (7) indicates that the input current can also be expressed as the sum of the input current contributed by each phase. The input current contributed by phase U, i.e., i_{EU}, can be formulated as follows:

$$i_{EU} = \frac{i_U v_U}{V_{DC}} = \frac{i_U}{V_{DC}} \frac{d\lambda_U}{dt} = \frac{i_U}{V_{DC}} \frac{d}{dt} \frac{\partial E'(\theta_E, i_U)}{\partial i_U}, \tag{8}$$

where λ_U is the magnetic flux linkage of the phase U, and t is the time. Equation (8) can be further developed as follows:

$$\begin{aligned} i_{EU} &= \frac{\Omega P_r}{V_{DC}} i_U \frac{d}{d\theta_E} \frac{\partial E'(\theta_E, i_U)}{\partial i_U} \\ &= \frac{\Omega P_r}{V_{DC}} \left[\frac{d}{d\theta_E} \left\{ i_U \frac{\partial E'(\theta_E, i_U)}{\partial i_U} \right\} - \frac{\partial E'(\theta_E, i_U)}{\partial i_U} \frac{di_U}{d\theta_E} \right], \end{aligned} \tag{9}$$

where Ω is the angular velocity of the rotor. By utilizing (6) and a relation as follows:

$$\frac{dE'(\theta_E, i_U)}{d\theta_E} = \frac{\partial E'(\theta_E, i_U)}{\partial \theta_E} + \frac{\partial E'(\theta_E, i_U)}{\partial i_U} \frac{di_U}{d\theta_E}, \tag{10}$$

i_{EU} can be rewritten as follows:

$$i_{EU} = \frac{\Omega P_r}{V_{DC}} \left[\frac{d}{d\theta_E} \left\{ i_U \frac{\partial E'(\theta_E, i_U)}{\partial i_U} - E'(\theta_E, i_U) \right\} + \frac{\tau_U(\theta_E, i_U)}{P_r} \right]. \tag{11}$$

Consequently, by substituting (3) into (11), i_{EU} can be formulated as follows:

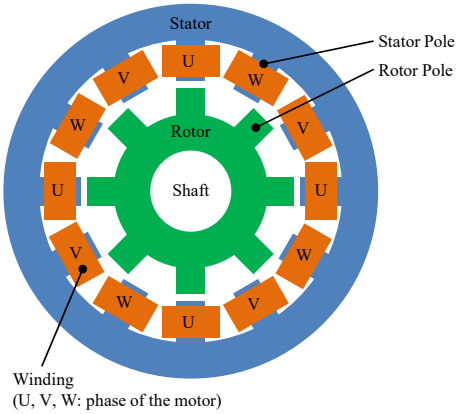

Fig. 1. Structure of three-phase concentrated-winding switched reluctance motor (SRM).

$$i_{EU}=\frac{\Omega P_r}{V_{DC}}\left[\frac{d}{d\theta_E}\left\{K_2(\theta_E)i_U^2\right\}+\frac{\tau_U(\theta_E,i_U)}{P_r}\right]. \tag{12}$$

Because of the symmetry among the three phases, the torque and the input current contributed by phases V and W must have the same waveforms as τ_U and i_{EU} with the phase shifts of $4\pi/3$ and $2\pi/3$, respectively. Therefore, both τ_U and i_{EU} should not contain harmonics of multiples of three to avoid ripples in the torque and input currents. However, the phase-current waveform causing such values of τ_U and i_{EU} is difficult to be directly derived based on the nonlinear relations between the phase current and τ_U, and between the phase current and i_{EU}. For the practical derivation of the phase-current waveform, the phase-current waveform is regarded as a function of the electrical angle θ_E. Then, two functions $g(\theta_E)$ and $p(\theta_E)$ are introduced to express τ_U and i_{EU} as linear equations of $g(\theta_E)$ and $p(\theta_E)$, as follows:

$$g(\theta_E)=K_2(\theta_E)i_U^2, \tag{13}$$

$$p(\theta_E)=g(\theta_E)\frac{\partial \ln K_2(\theta_E)}{\partial \theta_E}. \tag{14}$$

Using $g(\theta_E)$ and $p(\theta_E)$, τ_U and i_{EU} can be expressed as follows:

$$\tau_U(\theta_E)=P_r p(\theta_E), \tag{15}$$

$$i_{EU}(\theta_E)=\frac{\Omega P_r}{V_{DC}}\left\{\frac{dg(\theta_E)}{d\theta_E}+p(\theta_E)\right\}. \tag{16}$$

Because the phase current is regarded as a function of θ_E, τ_U and i_{EU} are also regarded as functions of θ_E. According to (15) and (16), the necessary condition for no ripples in the torque and the input current is that both $g(\theta_E)$ and $p(\theta_E)$ do not contain the harmonics of the multiples of three. Once such a pair of $g(\theta_E)$ and $p(\theta_E)$ is found, the phase current i_U that does not generate ripples in both the torque and the input current can be readily derived as follows:

$$i_U(\theta_E)=\sqrt{\frac{g(\theta_E)}{K_2(\theta_E)}}. \tag{17}$$

To derive the condition for no harmonics of the multiples of three in both $g(\theta_E)$ and $p(\theta_E)$, the origin of the electrical angle θ_E is taken at the aligned position of phase U, where the stator poles of phase U and rotor poles are aligned, and $g(\theta_E)$ and $\ln K_2(\theta_E)$ are assumed to have the forms as follows:

$$\begin{aligned} g(\theta_E)=&A_0+A_1\sin\theta_E+A_2\sin 2\theta_E+A_4\sin 4\theta_E\\ &+A_5\sin 5\theta_E+B_1\cos\theta_E+B_2\cos 2\theta_E\\ &+B_4\cos 4\theta_E+B_5\cos 5\theta_E, \end{aligned} \tag{18}$$

$$\begin{aligned} \ln K_2(\theta_E)=&k_0-k_1\cos\theta_E-\frac{k_2}{2}\cos 2\theta_E-\frac{k_3}{3}\cos 3\theta_E\\ &-\frac{k_4}{4}\cos 4\theta_E-\frac{k_5}{5}\cos 5\theta_E, \end{aligned} \tag{19}$$

where A_0–A_5 and B_1–B_5 are the coefficients characterizing $g(\theta_E)$, and k_0–k_5 are coefficients characterizing $\ln K_2(\theta_E)$. Because the phase inductance is an even function with respect to θ_E in many SRMs, $K_2(\theta_E)$ is assumed to be an even function of θ_E. The coefficients k_0–k_5 are given according to the SRM under consideration, and can be determined by calculating the Fourier's coefficients of $\ln\{L_U(\theta_E)/2\}$ according to (4).

The necessary conditions of the coefficients for no ripples in the torque and input currents can be determined by substituting (18) and (19) into (14) and seeking for the solution in which $p(\theta_E)$ does not have harmonic of multiples of three. As a result, the conditions are obtained as follows:

$$A_4=\frac{-\left\{k_4-k_2+(k_1-k_5)k_5/k_4\right\}A_1}{(k_1-k_5)\left(k_2/k_4-k_1k_5/k_4^2\right)+k_1-k_2k_5/k_4}, \tag{20}$$

$$A_2=-(k_5/k_4)A_1-\left(k_2/k_4-k_1k_5/k_4^2\right)A_4, \tag{21}$$

$$B_4=\frac{2k_3A_0+\left\{k_4+k_2-(k_1+k_5)k_5/k_4\right\}B_1}{(k_1+k_5)\left(k_2/k_4-k_1k_5/k_4^2\right)+k_1-k_2k_5/k_4}, \tag{22}$$

$$B_2=-(k_5/k_4)B_1-\left(k_2/k_4-k_1k_5/k_4^2\right)B_4, \tag{23}$$

$$A_5=-(k_5/k_4)A_4,\quad B_5=-(k_5/k_4)B_4. \tag{24}$$

Among the parameters A_0–A_5 and B_1–B_5, A_0, A_1, and B_1 can be chosen freely as far as $g(\theta_E)$ remains positive at any θ_E, whereas the others are determined according to (20)–(24). Therefore, this solution can derive various phase-current waveforms for achieving the simultaneous elimination of the torque and input-current ripples. This indicates that a preferable phase-current waveform can be chosen by optimizing a set of A_0, A_1, and B_1 according to a design requirement, e.g., the minimum root-mean-square value of the phase current for a given average output torque τ_{ave_prev}, which can be calculated as follows:

$$\tau_{ave\_prev}=\frac{3P_r}{2}(k_1A_1+k_2A_2+k_4A_4+k_5A_5). \tag{25}$$

Because (20)–(24) are linear relations among A_0–A_5 and B_1–B_5, an arbitrary attenuation or magnification of a solution of $g(\theta_E)$ and $p(\theta_E)$ is also a solution. Therefore, once a waveform of $i_U(\theta_E)$ that can eliminate both the torque and input-current ripples is derived according to (17), this waveform can be attenuated or magnified to adjust the average output torque without generating torque or input-current ripples.

III. Proposed Method

A. Overview of Proposed Method

The proposed method derives the phase-current waveform for eliminating the torque and input-current ripples by further considering the effect of the magnetic saturation. Similarly, as in the previous section, this section describes the proposed method based on the three-phase concentrated winding SRM, neglecting the magnetic coupling among the phases. However, in the proposed method (and similarly to [39] [40]), the magnetic co-energy is assumed to have a form for modeling the nonlinear flux-current relation owing to the magnetic saturation as follows:

$$E'_U(\theta_E, i_U) = K_2(\theta_E) i_U^2 + K_3(\theta_E) i_U^3 + \cdots + K_{m+1}(\theta_E) i_U^{m+1}, \tag{26}$$

where $K_2(\theta_E)$, $K_3(\theta_E)$, …, $K_{m+1}(\theta_E)$ are the coefficients according to the SRM under consideration. These coefficients characterize the dependence of the phase inductance on the phase current as follows:

$$\begin{aligned} L_U(\theta_E) &= \frac{\partial^2}{\partial i_U{}^2} E'_U(\theta_E, i_U) \\ &= 2K_2(\theta_E) + 6K_3(\theta_E) i_U + \cdots + m(m+1) i_U^{m-1}. \end{aligned} \tag{27}$$

Based on this modified co-energy, τ_U and i_{EU}, i.e., the torque and input current contributed by phase U, can be derived as follows:

$$\begin{aligned} \tau_U(\theta_E, i_U) = P_r \Bigg(& \frac{\partial K_2(\theta_E)}{\partial \theta_E} i_U^2 + \frac{\partial K_3(\theta_E)}{\partial \theta_E} i_U^3 \\ & + \cdots + \frac{\partial K_{m+1}(\theta_E)}{\partial \theta_E} i_U^{m+1} \Bigg), \end{aligned} \tag{28}$$

$$\begin{aligned} i_{EU}(\theta_E, i_U) = \frac{\Omega}{V_{dc}} \Bigg[& \frac{d}{d\theta_E} \left\{ K_2(\theta_E) i_U^2 + 2K_3(\theta_E) i_U^3 \right. \\ & \left. + \cdots + m K_{m+1}(\theta_E) i_U^{m+1} \right\} + \tau_U(\theta_E) \Bigg] \end{aligned} \tag{29}$$

Because of the symmetry among the phases, the harmonics of the multiples of three in τ_U and i_{EU}, defined in (28) and (29), cause the torque and input-current ripples. Consequently, the purpose of the proposed method is to find an i_U that can eliminate the harmonics of the multiples of three from both (28) and (29). However, according to (28) and (29), τ_U and i_{EU} are not linear functions of i_U nor $i_U{}^2$, making direct calculation of the solution difficult. Therefore, the proposed method adopts an asymptotic approach to the solution instead.

Fig. 2 depicts the phase-current waveform derivation procedure of the proposed method. This procedure starts from deriving the phase-current waveform for the predetermined average output torque according to the previous method [36] reviewed in the previous section (which indicates that the magnetic saturation is provisionally neglected). As reviewed in the previous section, the derivation of the phase current waveform of the previous method determines parameters A_0–A_5 and B_1–B_5 in (18) for the predetermined average output torque, and then derives the phase current $i_U(\theta_E)$ using these parameters according to (17). However, as reviewed in the previous section, this waveform can eliminate the torque and input-current ripples only under the condition of lacking the magnetic nonlinearity caused by the magnetic saturation. Therefore, despite this waveform, the harmonics of the multiples of three in τ_U and i_{EU} remain under the condition with the magnetic saturation, thereby generating the torque and input-current ripples. Therefore, based on this waveform, the next step searches for a slightly modified phase-current waveform that can further eliminate the harmonics of the multiples of three from τ_U and i_{EU} without affecting the average output torque. This slightly modified waveform is derived by considering the magnetic saturation based on the magnetic co-energy model of (26), according to the analytical method described in the next subsection. This step can be repeated to further slightly modify the input phase-current waveform in each time of repetition. This can furthre reduce the remaining harmonics of the multiples of three from τ_U and i_{EU}, thus finally obtaining the phase-current waveform for sufficiently eliminating the torque and input-current ripples under the magnetic saturation.

The following subsection describes the detailed analytical calculation method of this step, and derives the slightly modified phase-current waveform $i_{MU}(\theta_E)$ from the input phase-current waveform $i_{BU}(\theta_E)$. As this method needs the modeling parameters for the nonlinear magnetic co-energy, i.e., of $K_2(\theta_E)$, $K_3(\theta_E)$, …, and $K_{m+1}(\theta_E)$, the determination method of these

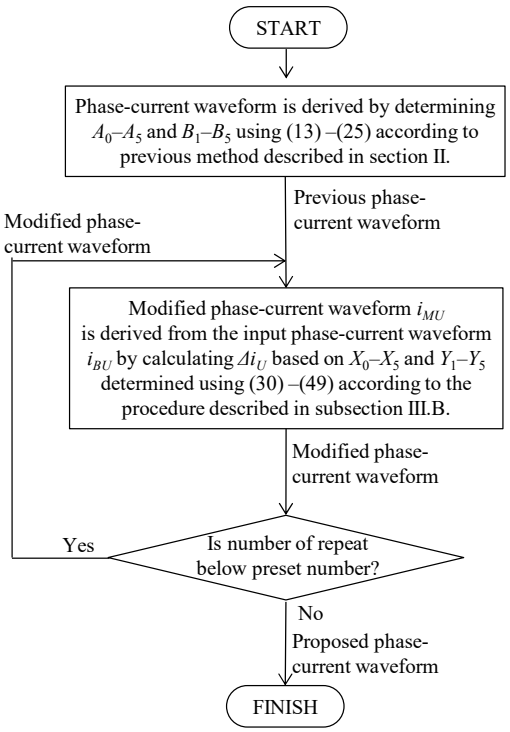

Fig. 2. Procedure of proposed phase-current derivation method.

parameters for an actual SRM is described in subsection III.C.

B. Derivation of Modified Phase-Current Waveform

Let i_{BU} and i_{MU} be the input phase-current waveform to this step and the resultant slightly modified phase-current waveform derived by this step, respectively. The relation between i_{BU} and i_{MU} can be expressed as follows:

$$i_{MU}(\theta_E) = i_{BU}(\theta_E) + \Delta i_U(\theta_E), \tag{30}$$

where $\Delta i_U(\theta_E)$ is the small deviation of i_{MU} from i_{BU}. In this discussion, Δi_U is assumed to have a far smaller amplitude than i_{MU} and i_{BU}. By substituting i_{MU} into i_U in (28) and (29), and ignoring the terms of order higher than the second in Δi_U, τ_U and i_{EU} can be expressed as the linear equations of Δi_U as follows:

$$\tau_U(\theta_E) = P_r\{q(\theta_E) + f(\theta_E)\Delta i_U(\theta_E)\}, \tag{31}$$

$$i_{EU}(\theta_E) = \frac{\Omega P_r}{V_{dc}}\left[\frac{d}{d\theta_E}\{e(\theta_E) + h(\theta_E)\Delta i_U(\theta_E)\} + \frac{\tau_U(\theta_E)}{P_r}\right], \tag{32}$$

where $q(\theta_E)$, $f(\theta_E)$, $e(\theta_E)$, and $h(\theta_E)$ are given functions of θ_E, and are defined as follows:

$$\begin{aligned} q(\theta_E) = {} & \frac{\partial K_2(\theta_E)}{\partial \theta_E} i_{BU}^2(\theta_E) + \frac{\partial K_3(\theta_E)}{\partial \theta_E} i_{BU}^3(\theta_E) \\ & + \cdots + \frac{\partial K_{m+1}(\theta_E)}{\partial \theta_E} i_{BU}^{m+1}(\theta_E), \end{aligned} \tag{33}$$

$$\begin{aligned} f(\theta_E) = {} & 2\frac{\partial K_2(\theta_E)}{\partial \theta_E} i_{BU}(\theta_E) + 3\frac{\partial K_3(\theta_E)}{\partial \theta_E} i_{BU}^2(\theta_E) \\ & + \cdots + (m+1)\frac{\partial K_{m+1}(\theta_E)}{\partial \theta_E} i_{BU}^m(\theta_E), \end{aligned} \tag{34}$$

$$\begin{aligned} e(\theta_E) = {} & K_2(\theta_E) i_{BU}^2(\theta_E) + 2K_3(\theta_E) i_{BU}^3(\theta_E) \\ & + \cdots + mK_{m+1}(\theta_E) i_{BU}^{m+1}(\theta_E), \end{aligned} \tag{35}$$

$$\begin{aligned} h(\theta_E) = {} & 2K_2(\theta_E) i_{BU}(\theta_E) + 6K_3(\theta_E) i_{BU}^2(\theta_E) \\ & + 12K_4(\theta_E) i_{BU}^3(\theta_E) + \cdots + m(m+1)K_{m+1}(\theta_E) i_{BU}^m(\theta_E). \end{aligned} \tag{36}$$

Let $s(\theta_E)$ and $l(\theta_E)$ be functions of θ_E defined as follows:

$$s(\theta_E) = q(\theta_E) + f(\theta_E)\Delta i_U(\theta_E), \tag{37}$$

$$l(\theta_E) = e(\theta_E) + h(\theta_E)\Delta i_U(\theta_E). \tag{38}$$

Then, the sufficient condition for simultaneous elimination of the torque and input-current ripples can be expressed as that both $s(\theta_E)$ and $l(\theta_E)$ must not contain the harmonics of the multiples of three. Consequently, $\Delta i_U(\theta_E)$ should be determined such that it eliminates the harmonics of multiples of three from $s(\theta_E)$ and $l(\theta_E)$.

To search for such $\Delta i_U(\theta_E)$, an equation is obtained by eliminating $\Delta i_U(\theta_E)$ from (37) and (38), as follows:

$$s(\theta_E) = g(\theta_E) l(\theta_E) + k(\theta_E), \tag{39}$$

where $g(\theta_E)$ and $k(\theta_E)$ are functions of θ_E defined as follows:

$$g(\theta_E) = \frac{f(\theta_E)}{h(\theta_E)}, \quad k(\theta_E) = q(\theta_E) - \frac{f(\theta_E) e(\theta_E)}{h(\theta_E)}. \tag{40}$$

Notably, $g(\theta_E)$ and $k(\theta_E)$ are given functions, because these functions can be readily calculated from the given magnetic co-energy model of (26), and the original phase-current waveform $i_{BU}(\theta_E)$ according to (33)–(36). Therefore, a pair of $s(\theta_E)$ and $l(\theta_E)$ should be determined such that they do not contain the harmonics of multiples of three under the given functions of $g(\theta_E)$ and $k(\theta_E)$. Once such a pair of $s(\theta_E)$ and $l(\theta_E)$ is found, the desired $\Delta i_U(\theta_E)$ can be readily calculated as follows:

$$\Delta i_U(\theta_E) = \frac{l(\theta_E) - e(\theta_E)}{h(\theta_E)}. \tag{41}$$

For simplifying the calculation for determining $\Delta i_U(\theta_E)$, $g(\theta_E)$ and $k(\theta_E)$ can approximated to have the following forms by neglecting the harmonics of θ_E higher than six, as follows:

$$\begin{aligned} g(\theta_E) \approx {} & C_0 + C_1\cos\theta_E + C_2\cos 2\theta_E + C_3\cos 3\theta_E \\ & + C_4\cos 4\theta_E + C_5\cos 5\theta_E + C_6\cos 6\theta_E \\ & + D_1\sin\theta_E + D_2\sin 2\theta_E + D_3\sin 3\theta_E \\ & + D_4\sin 4\theta_E + D_5\sin 5\theta_E + D_6\sin 6\theta_E, \end{aligned} \tag{42}$$

$$\begin{aligned} k(\theta_E) \approx {} & T_0 + T_1\cos\theta_E + T_2\cos 2\theta_E + T_3\cos 3\theta_E \\ & + T_4\cos 4\theta_E + T_5\cos 5\theta_E + T_6\cos 6\theta_E \\ & + U_1\sin\theta_E + U_2\sin 2\theta_E + U_3\sin 3\theta_E \\ & + U_4\sin 4\theta_E + U_5\sin 5\theta_E + U_6\sin 6\theta_E, \end{aligned} \tag{43}$$

where C_0–C_6, D_1–D_6, T_0–T_6, and U_1–U_6 are the Fourier coefficients extracted by applying the Fourier series expansion to $g(\theta_E)$ and $k(\theta_E)$. Furthermore, remembering that $l(\theta_E)$ should not contain the harmonics of multiples of three, $l(\theta_E)$ is simply assumed to have a form as follows:

$$\begin{aligned} l(\theta_E) = {} & X_0 + X_1\cos\theta_E + X_2\cos 2\theta_E + X_4\cos 4\theta_E \\ & + X_5\cos 5\theta_E + Y_1\sin\theta_E + Y_2\sin 2\theta_E \\ & + Y_4\sin 4\theta_E + Y_5\sin 5\theta_E. \end{aligned} \tag{44}$$

In the above, X_0–X_5 and Y_1–Y_5 are the Fourier coefficients to be determined.

Substituting (42)–(44) into (39) yields the required conditions of the coefficients X_0–X_5 and Y_1–Y_5 for eliminating the harmonics of multiples of three from $s(\theta_E)$. Consequently, the required conditions of these coefficients are obtained as follows:

$$
\begin{aligned}
X_4 = -\{&2D_2U_6 + 2D_1U_3 + 2C_2T_6 - 2C_1T_3 + 2X_0D_2D_6 \\
&+ (X_1D_2 + X_2D_1 - Y_1C_2 - Y_2C_1)D_5 \\
&+ (X_2D_2 + X_1D_1 - Y_2C_2 - Y_1C_1)D_4 + 2X_0D_1D_3 \\
&+ (X_1D_1 + Y_1C_5 + Y_2C_4 + Y_1C_1)D_2 + X_2D_1^2 \\
&+ (-Y_2C_5 + Y_1C_4 + Y_1C_2 + 2Y_2C_1)D_1 + 2X_0C_2C_6 \\
&+ (X_1C_2 - X_2C_1)C_5 + (X_2C_2 - X_1C_1)C_4 - 2X_0C_1C_3 \\
&- X_1C_1C_2 - X_2C_1^2\}/(D_2^2 - D_1^2 + C_2^2 - C_1^2).
\end{aligned} \tag{45}
$$

$$
\begin{aligned}
X_5 = \{&2D_1U_6 + 2D_2U_3 + 2C_1T_6 - 2C_2T_3 + 2X_0D_1D_6 \\
&+ (X_2D_2 + X_1D_1 - Y_2C_2 - Y_1C_1)D_5 \\
&+ (X_1D_2 + X_2D_1 - Y_1C_2 - Y_2C_1)D_4 + 2X_0D_2D_3 \\
&+ (X_2D_1 - Y_2C_5 - Y_1C_4 + 2Y_1C_2 + Y_2C_1)D_2 + X_1D_2^2 \\
&+ (Y_1C_5 + Y_2C_4 + Y_2C_2)D_1 + 2X_0C_1C_6 \\
&+ (X_1C_1 - X_2C_2)C_5 + (X_2C_1 - X_1C_2)C_4 - 2X_0C_2C_3 \\
&- X_2C_1C_2 - X_1C_2^2\}/(D_2^2 - D_1^2 + C_2^2 - C_1^2).
\end{aligned} \tag{46}
$$

$$
\begin{aligned}
Y_4 = -\{&2C_2U_6 - 2C_1U_3 - 2D_2T_6 - 2D_1T_3 + 2X_0C_2D_6 \\
&+ (Y_1D_2 - Y_2D_1 + X_1C_2 - X_2C_1)D_5 \\
&+ (Y_2D_2 - Y_1D_1 + X_2C_2 - X_1C_1)D_4 - 2X_0C_1D_3 \\
&+ (Y_1D_1 - 2X_0C_6 - X_1C_5 - X_2C_4 - X_1C_1)D_2 + Y_2D_1^2 \\
&+ (-X_2C_5 - X_1C_4 - 2X_0C_3 - X_1C_2 - 2X_2C_2)D_1 \\
&+ (Y_1C_2 + Y_2C_1)C_5 + (Y_2C_2 + Y_1C_1)C_4 - Y_1C_1C_2 \\
&- Y_2C_1^2\}/(D_2^2 - D_1^2 + C_2^2 - C_1^2),
\end{aligned} \tag{47}
$$

$$
\begin{aligned}
Y_5 = \{&2C_1U_6 - 2C_2U_3 - 2D_1T_6 - 2D_2T_3 + 2X_0C_1D_6 \\
&+ (-Y_2D_2 + Y_1D_1 - X_2C_2 + X_1C_1)D_5 + Y_1D_2^2 \\
&+ (-Y_1D_2 + Y_2D_1 - X_1C_2 + X_2C_1)D_4 - 2X_0C_2D_3 \\
&+ (-X_2C_5 - X_1C_4 - 2X_0C_3 - X_1C_2 - 2X_2C_2)D_1 \\
&+ (Y_2D_1 - X_2C_5 - X_1C_4 - 2X_0C_3 - 2X_1C_2 - X_2C_1)D_2 \\
&+ (-2X_0C_6 - X_1C_5 - X_2C_4 - X_2C_2)D_1 \\
&+ (Y_2C_2 + Y_1C_1)C_5 + (Y_1C_2 + Y_2C_1)C_4 - Y_2C_1C_2 \\
&- Y_1C_2^2\}/(D_2^2 - D_1^2 + C_2^2 - C_1^2).
\end{aligned} \tag{48}
$$

These requirement conditions (45)–(48) can determine a pair of $s(\theta_E)$ and $l(\theta_E)$ by choosing an arbitrary set of five parameters X_0–X_2, Y_1, and Y_2. Then, Δi_U can be readily determined according to (41), finally obtaining the slightly modified phase-current waveform i_{MU} according to (30). Therefore, there are a variety of values for i_{MU}, owing to the variety of possible sets of X_0–X_2, Y_1, and Y_2. Nonetheless, a set X_0–X_2, Y_1, and Y_2 should be chosen such that the resultant waveform i_{MU} generates the same output torque as the previous waveform i_{BU}. The average torque τ_{ave_modi} generated by i_{MU} can be calculated as follows:

$$
\begin{aligned}
\tau_{ave\_modi} = \frac{3P_r}{2}&(2T_0 + 2C_0X_0 + C_1X_1 + C_2X_2 + C_4X_4 \\
&+ C_5X_5 + D_1Y_1 + D_2Y_2 + D_4Y_4 + D_5Y_5).
\end{aligned} \tag{49}
$$

There still remains a variety of possible sets for X_0–X_2, Y_1, and Y_2. Choosing a preferable set is dependent on the design strategy. For example, in this study, the parameter set was chosen such that the root-mean-square ratio of Δi_U to i_{BU} is at a minimum to have a small Δi_U compared to i_{BU}, which is assumed for deriving (31) and (32).

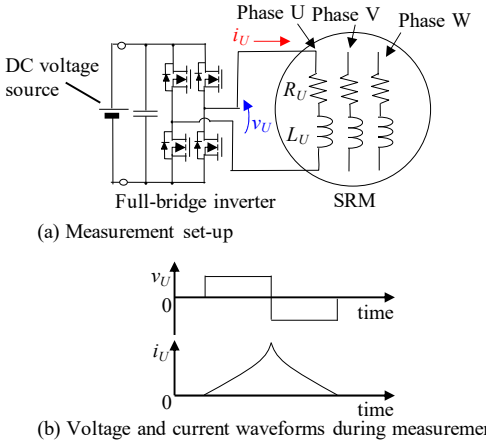

Fig. 3. Measurement method of relation between phase flux linkage and phase current.

Notably, significant approximation is contained in this derivation method of the slightly modified phase-current waveform i_{MU}. Therefore, in a case where the resultant phase-current waveform does not sufficiently eliminate the torque and input-current ripples, this process can be repeated to improve the reduction of the ripples.

C. Parameter Extraction for Nonlinear Co-Energy Model

For performing the proposed method of deriving the phase-current waveform, the parameters $K_2(\theta_E)$–$K_{m+1}(\theta_E)$ must be determined for the SRM under consideration. This subsection describes the practical determination method for these parameters, based on the SRM modeling method proposed in [39].

First, the relation between the phase flux linkage λ_U and the phase current i_U was measured at various electrical angles. For this purpose, the square voltage waveform $v_U(t)$ was applied to the winding of phase U while the rotor was mechanically fixed at a predetermined electrical angle and the other phase windings were kept open, as shown in Fig. 3. Simultaneously, the phase current waveform $i_U(t)$ and voltage waveform $v_U(t)$ were measured. By utilizing the measurement result, the phase flux linkage waveform $\lambda_U(t)$ was obtained, as follows:

$$
\lambda_U(t) = \int v_U - R_U i_U \, dt, \tag{50}
$$

where R_U is the parasitic resistance of the winding of phase U. Based on $\lambda_U(t)$ and $i_U(t)$, the phase flux linkage was obtained as the function of the phase current; it was the relation between the phase flux linkage λ_U and phase current i_U at this electrical angle. Therefore, by repeating this experiment at various electrical angles, the full database of the relations between λ_U and i_U was obtained.

Second, the magnetic co-energy contributed by phase U, i.e.,

$E'_U(\theta_E, i_U)$, was determined as a function of the electrical angle θ_E and phase current i_U. The magnetic co-energy was calculated based on the measured relation between the phase flux linkage λ_U and phase current i_U, as follows:

$$E'_U(\theta_E, i_U) = i_U \lambda_U(\theta_E, i_U) - \int \lambda_U(\theta_E, i_U) di_U. \quad (51)$$

Third, the parameters of $K_2(\theta_E)$, $K_3(\theta_E)$, …, $K_{m+1}(\theta_E)$ were extracted from $E'_U(\theta_E, i_U)$. The parameters were obtained by applying a multiple regression analysis to expand the magnetic co-energy into a form as follows:

$$E'_U(\theta_E, i_U) = K_2(\theta_E) i_U^2 + K_3(\theta_E) i_U^3 + \cdots + K_{m+1}(\theta_E) i_U^{m+1}. \quad (52)$$

The resultant parameters $K_2(\theta_E)$, $K_3(\theta_E)$, …, $K_{m+1}(\theta_E)$ contained the high-order harmonics caused by the measurement error of v_U and i_U, as well as the estimation error in the multiple regression analysis. For filtering out these high-order harmonics, the resultant parameters $K_2(\theta_E)$, $K_3(\theta_E)$, …, $K_{m+1}(\theta_E)$ were further applied with a Fourier series expansion, and by neglecting the terms of order higher than six, were fit into the form as follows:

$$K_n(\theta_E) = K_{n0} + K_{n1}\cos\theta_E + K_{n2}\cos 2\theta_E + \cdots + K_{n6}\cos 6\theta_E, \quad (53)$$

where K_{n0}, K_{n1}, K_{n2}, …, K_{n6} are the Fourier series coefficients, and n is a natural number ranging from 2 to m+1. Because the phase inductance is an even function with respect to θ_E in many SRMs, $K_2(\theta_E)$, $K_3(\theta_E)$, …, $K_{m+1}(\theta_E)$ were assumed to be even functions.

IV. Simulation

A simulation was performed to evaluate the effectiveness of the phase current waveform derived by the proposed method. In this simulation, a two-dimensional FEM-based electromagnetic analysis was conducted using a commercial simulator JMAG-Designer 18.1 (JSOL Corp.) for evaluating the operation of the SRM under magnetic saturation.

The SRM simulation model was constructed based on a commercially available SRM, whose specifications are listed in Table I. The materials used in the model are listed in Table II. This model incorporated the magnetic saturation property of the material, although the model did not incorporate the copper loss and iron loss. The reason for not incorporating the copper loss and the iron loss was that the purpose of this simulation was to examine the theoretical appropriateness of the proposed method, which derives the phase current waveform under the approximation that these losses are negligible.

Fig. 4(a) and Fig. 4(b) present the geometry of the SRM model and computational mesh generated for the FEM simulation, respectively. The mesh size was particularly small near the gap between the stator and the rotor. The typical mesh was 0.15 mm near the gap, and 2.0 mm in the back yoke of the stator.

TABLE I
Specifications of SRM Used for Simulation and Experiment

Model number	RB165SR-96CSRM (Motion System Tech. Inc.)
Rated value	1.2 kW, 96 V, 6000 r/min
Structure	Stator: 12 poles, Rotor: 8 poles, Number of turns: 14 tunes/pole Outer diameter of stator: 136 mm Outer diameter of rotor: 83 mm Gap between stator and rotor: 0.3 mm Diameter of shaft: 25 mm Stack length: 40 mm
Material	35H300 (Nippon Steel Corp.)
Characteristics	Maximum reluctance R_{max}: 4.1×10^6 A/Wb (Minimum inductance: 0.2 mH) Minimum reluctance R_{min}: 0.5×10^6 A/Wb (Maximum inductance: 1.5 mH)

TABLE II
Materials Utilized in Simulation Model

Component	Material name or relative magnetic permeability
Stator	Material name: 35H300 (Nippon Steel Corp.)
Rotor	Material name: 35H300 (Nippon Steel Corp.)
Winding	Relative magnetic permeability: 1
Shaft	Relative magnetic permeability: 1

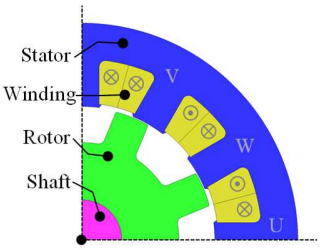

(a) Geometry of simulation model

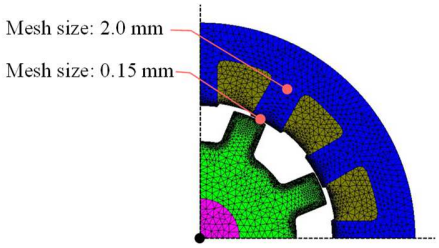

(b) Computational mesh

Fig. 4. Two-dimensional simulation model of SRM.

In this simulation, the three types of phase-current waveforms were applied to the phase windings using the current source to evaluate and compare the torque and input-current ripples. The first one was the phase-current waveform derived by the proposed method. The second one was the phase-current waveform derived by the previous method [36], which does not consider the magnetic saturation. The third one was a traditional square-shape phase-current waveform, whose firing and extinction angles were tuned to minimize the torque ripple considering the magnetic saturation as well as the root-mean-square of the phase current, as described in Subsection IV.A. Unlike the actual motor driving system, which utilizes the inverter to magnetize the motor, this simulation utilized the

current source to magnetize the motor. Therefore, the phase current waveforms of this simulation did not contain the switching ripple of the inverter, thus enabling evaluation of the torque and input-current ripples without contamination of the switching ripple. The simulation was executed for every degree of the electrical angle.

Hereafter, the torque and input-current ripples were compared using the ripple ratios, defined as their peak-to-peak values normalized by their average values, as follows:

$$\tau_{ripple} = \frac{\tau_{pp}}{\tau_{ave}}, \quad i_{E\_ripple} = \frac{i_{E\_pp}}{i_{E\_ave}}, \tag{54}$$

where τ_{ripple} and i_{E_ripple} are the ripple ratios of the torque and input current, respectively; τ_{pp} and i_{E_pp} are the peak-to-peak values of the torque and input current, respectively; and τ_{ave} and i_{E_ave} are the average values of the torque and input current, respectively.

The torque and input-current ripples were evaluated at the rotational speeds 250 r/min and 2000 r/min, respectively, under an output torque of 5 N·m. This output torque was chosen as a representative torque of the SRM under consideration where the magnetic saturation severely affected the operation under the phase-current waveform of the previous method [36], as reported in [37]. The rotational speeds of 250 r/min and 2000 r/min were chosen as representative speeds for EV propulsion motors.

A. Derivation of Phase-Current Waveforms

The phase-current waveform of the previous method [36] was derived by adopting the incremental inductance at the phase current of 5 A as $2K_2(\theta_E)$ in (3). As discussed in Section II, there are a variety of possible phase-current waveforms. Therefore, the preferable waveform was chosen such that the waveform had the minimum root-mean-square value for a given output torque. This waveform was then magnified to adjust the average torque, because the actual output torque became smaller than the theoretically predicted average torque τ_{ave_prev} owing to the magnetic saturation.

Next, the phase-current waveform of the proposed method was derived. For the derivation of the phase current waveform, $K_2(\theta_E)$, $K_3(\theta_E)$, …, $K_{m+1}(\theta_E)$ of the SRM under consideration were extracted according to the method described in Subsection III.C, i.e., by simulating the phase-current waveform when the phase winding was applied with the square voltage waveform as shown in Fig. 3. The integer m in (26) was set to 6. Then, the phase current was derived by adopting the phase-current waveform of the previous method [36] as i_{BU}. As discussed in Subsection III.B, there are a variety of modified phase-current waveforms i_{MU}. Therefore, the preferable waveform was chosen such that the root-mean-square of Δi_U was minimum. The modification process was passed twice before obtaining the final phase-current waveform.

The square-shape phase-current waveform was derived by adjusting the firing angle θ_{on}, extinction angle θ_{off}, and peak value I_{peak} to output the desired torque while minimizing an evaluation function ζ. The evaluation function ζ represented the root-mean-square of the phase current and torque ripple, as follows:

$$\zeta\left(\theta_{on}, \theta_{off}, I_{peak}\right) = 0.5\frac{I_{rms}}{I_{rms\_\min}} + 0.5\frac{\tau_{ripple}}{\tau_{ripple\_\min}}, \tag{55}$$

where I_{rms} is the root-mean-square value of the phase current; and $I_{rms\_\min}$ and $\tau_{ripple\_\min}$ are the minimum possible values of I_{rms} and τ_{ripple}, respectively, that can be achieved by adjusting θ_{on}, θ_{off}, and I_{peak} at the desired torque output. Additionally, θ_{on} and θ_{off} were chosen so that the electrical angle difference between θ_{on} and θ_{off} was equal or greater than 120 degrees, so as not to have excessively large sharp spikes in the input current during the commutation between the phases.

In an actual motor driving system, the rising and falling transient of the phase current is restricted by the DC voltage of the inverter, and deforms the actual phase current waveform depending on the rotational speed. Therefore, the evaluation function ζ was calculated under the restriction that the maximum time derivative of the magnetic flux linkage of each phase was 96 V, i.e., the rated voltage of the SRM under consideration. Consequently, θ_{on}, θ_{off}, and I_{peak} were determined as 215 degrees, 360 degrees, and 51 A for 250 r/min, respectively; they were determined as 215 degrees, 360 degrees, and 52 A for 2000 r/min, respectively.

Consequently, the three phase-current waveforms to be tested were determined as shown in Fig. 5(a). The phase-current waveforms of the proposed method and the previous method [36] each had a root-mean-square value approximately 1.45 times as large as the square-shape phase-current waveform if compared at the rotation speed of 250 r/min. This large root-

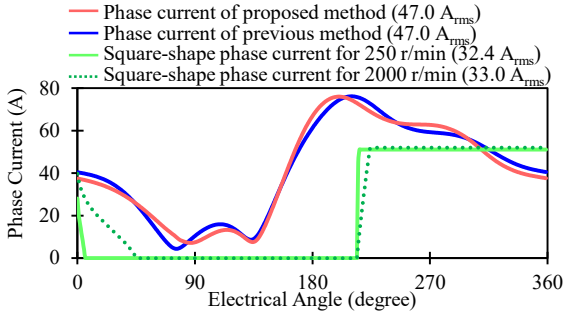

(a) Phase-current waveform

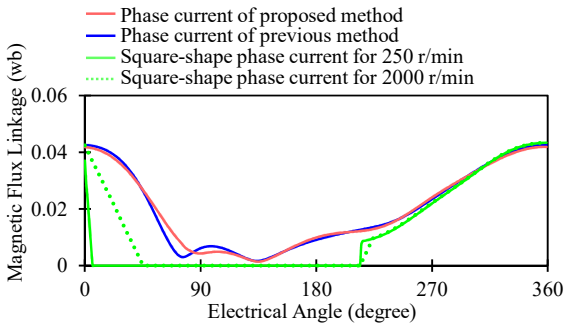

(b) Flux linkage waveform

Fig. 5. Phase-current and flux linkage waveforms derived for simulation.

mean-square value was not preferable because of large copper loss. However, this drawback was partly caused by adopting the commercially available SRM for the application of the proposed method and previous method [36]. The commercially available SRM was generally designed to be driven with the square-shape phase-current waveform, and therefore was not optimized for the proposed method and previous method [36]. Actually, as for the previous method, [36] and [37] revealed the effectiveness of tuning the rotor geometry for reduction of the root-mean-square value of the phase-current waveform, without deteriorating the ripple reduction effect of the torque and input currents. Therefore, this drawback of the proposed method, i.e., the large root-mean-square of the phase-current, can be expected to be mitigated by developing an optimization method for the physical SRM structure.

Fig. 5(b) shows the flux linkage waveforms calculated based on Fig. 5(a). As can be seen in the figure, the phase current waveform of the proposed method has a similar peak flux linkage value as that of the previous method and the square-shaped phase-current waveform. As a result, these three phase-current waveforms cause similar levels of magnetic saturation, as can be inferred from the magnetic flux density distribution at the electrical angles of the peak flux linkage, as shown in Fig. 6.

B. Torque and Input-Current Ripples

Fig. 7 presents the simulation results at the rotation speed of 250 r/min. The ripple ratios of the torque ripple and input-current ripple are also presented in Fig. 7(a) and Fig. 7(b), respectively. The torque ripple ratios of the proposed method, previous method [36], and square-shape phase current are 35%, 54%, and 28%, respectively. Meanwhile, the input-current ripple ratios of the proposed method, previous method [36], and square-shape phase-current are 103 %, 206 %, and 3609 %, respectively. These results indicate that the proposed method exhibits excellent suppression of both the torque and input-current ripples at this rotation speed, as is expected from the theory.

The effectiveness of the proposed method was also shown in the simulation results at the rotation speed of 2000 r/min, which are presented in Fig. 8. The ripple ratios of the torque ripple and the input-current ripple are also presented in Fig. 8(a) and Fig. 8(b), respectively. The torque ripple ratios of the proposed method, previous method [36], and square-shape phase-current are 35%, 54%, and 38%, respectively. Meanwhile, the input-current ripple ratios of the proposed method, previous method [36], and square-shape phase-current are 103%, 206%, and 730%, respectively. Consequently, the simulation supports the effectiveness of the proposed method in deriving a phase-current waveform with smaller torque and input-current ripples under the magnetic saturation.

As can be seen in Fig. 7 and Fig. 8, the phase-current waveform of the proposed method still generates small ripples in both the torque and input current. The reason for the remaining ripples is not clarified herein. Nonetheless, these ripples might be caused by a modeling error caused by approximating the nonlinear characteristic of the magnetic co-

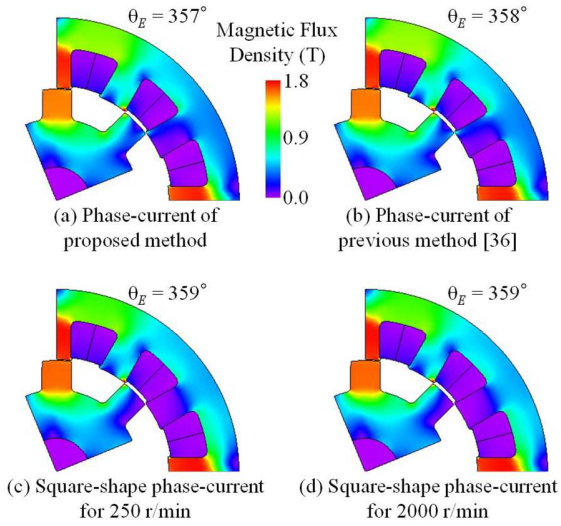

Fig. 6. Magnetic flux density distribution at the electrical angle where the maximum flux linkage was generated.

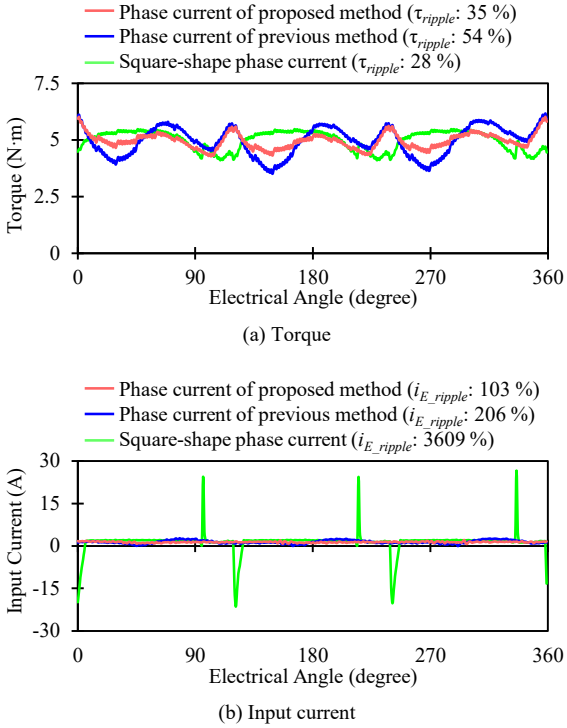

Fig. 7. Simulation results at 250 r/min.

energy using a limited number of parameters, i.e., $K_2(\theta_E)$, $K_3(\theta_E)$, …, $K_7(\theta_E)$, and approximating these parameters in the form of (53). The ripples might also be caused by the limited order of the Fourier series expansion of $g(\theta_E)$ and $k(\theta_E)$. Besides, the limited repetition of the derivation process of the modified phase-current waveform i_{MU} may have resulted in the insufficient optimization of the phase-current waveform. Therefore, the remaining ripples may be further reduced by considering higher orders for approximating the magnetic co-energy as well as the parameters $K_2(\theta_E)$, …, $K_{m+1}(\theta_E)$, $g(\theta_E)$, and $k(\theta_E)$, and by additional repetitions of the derivation process of i_{MU} for better optimization of the phase-current waveform.

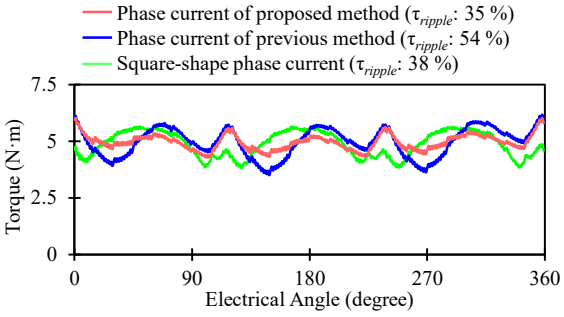

(a) Torque

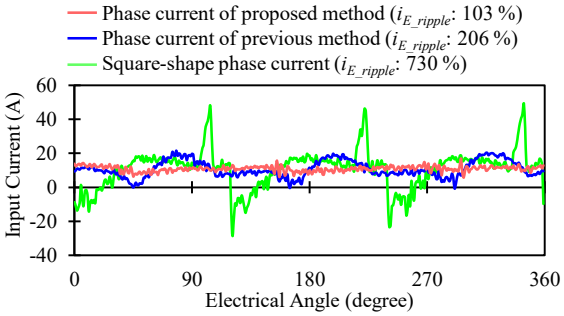

(b) Input current

Fig. 8. Simulation results at 2000 r/min.

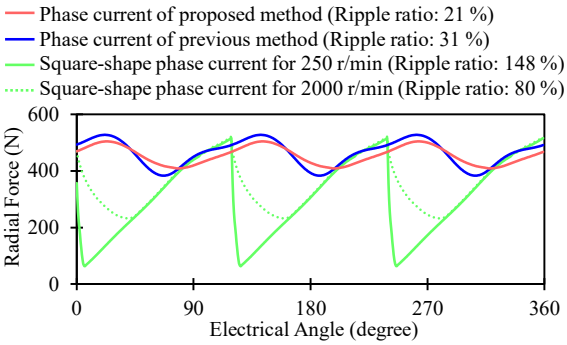

Fig. 9. Simulation results of radial force.

C. *Radial Force Ripple*

Fig. 9 presents the simulation results for the radial force based on the phase current waveforms presented in Fig. 5. The radial force was calculated according to the method described in [41]. This figure also presents the ripple ratios of the radial force. The results reveal that the proposed method exhibits the smallest radial force ripple among the proposed method, previous method [36], and square-shape phase-current for both 250 r/min and 2000 r/min. As pointed out in [4][5], the ripple in the radial force is a major cause of the acoustic noise in a motor propulsion system. Therefore, this result implies that the proposed method is also effective for mitigating acoustic noise in addition to the torque and input-current ripples.

V. Experiment

An experiment was performed to evaluate the torque and input-current ripple reduction effect by the proposed method.

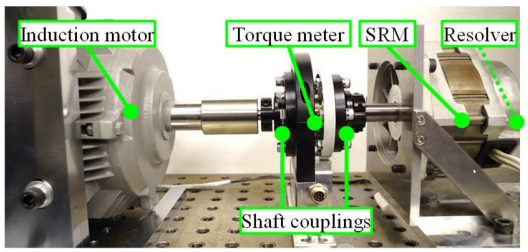

(a) Motor test bench

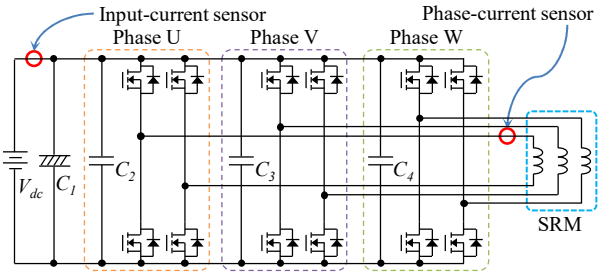

DC power supply (V_{dc}): GPO250-20R (Takasago)
Power MOS-FETs: IRFP4668PBF (International Rectifier)
C_1: LQR2W562MSEJ (5.6 mF, Nichicon)
C_2, C_3, C_4: C4AEGBW6100A3NJ (100 μF, KEMET)
CKG57NX7T2W225M500JH (TDK) × 2

(b) Schematic diagram of three-phase H-bridge inverter for SRM drive

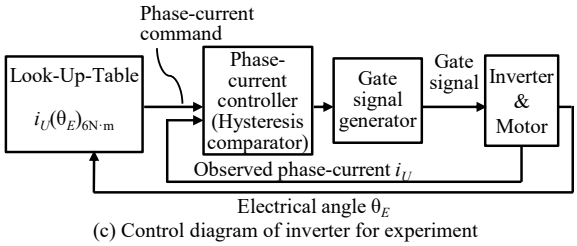

(c) Control diagram of inverter for experiment

Fig. 10. Experimental set-up.

TABLE III
Specifications of Motor Test Bench

Instrument	Specifications
SRM	Model: RB165SR-96CSRM (Motion System Tech. Inc.) Rate: 1.2 kW, 96 V, 6000 r/min Structure: Stator: 12 poles, Rotor: 8 poles, Number of turns: 14 turns/pole
Resolver	TS2224N1114E102 (Tamagawa Seiki Co., Ltd.) Precision: ±0.5 deg.
Torque meter	T40B 50Nm (HBM Corp.) Sensitivity Tolerance: ±0.1 %
Shaft Coupling	SFF-060SS-T059N (Miki Pulley co., LTD.) SFF-060SS-T060N (Miki Pulley co., LTD.)
Induction motor	TFO-K 3.7kW 2P 200V (Hitachi Industrial Equipment Systems Co., LTD.)

This experiment employed the commercial SRM used in the simulation, whose specifications are listed in Table I. In this experiment, the torque and input-current ripples were compared among the three phase-current waveforms, i.e., the phase-current waveform of the proposed method, that of the previous method [36], and the square-shape phase current.

Fig. 10 shows the experimental setup employed for this experiment. Fig. 10(a) is the photograph of the motor test bench, whose specifications are listed in Table III. The SRM was mechanically connected to an induction motor used as a mechanical load via shaft couplings and a torque meter. A resolver was attached to the end of the rotor of the SRM to detect the mechanical angle.

The SRM was driven by the three-phase full-bridge inverter, whose schematic diagram is shown in Fig. 10(b). This inverter was supplied with the DC power with the voltage of 96 V. The phase current was controlled by the inverter using hysteresis control. Fig. 10(c) shows the control diagram. This control was implemented in the commercial digital signal processor-based control system PE-Expert3 (Myway Plus Corp.). The reference phase-current waveforms were stored in look-up-tables as functions of the electrical angle. The hysteresis width was set at 7 A.

The maximum possible switching frequency was restricted by the sampling frequency of the phase current, which was approximately 2.8 MHz. However, the average switching frequency in the experiment at the rotation speed of 250 r/min was observed as 12.2 kHz for the phase-current waveform of the proposed method, 11.8 kHz for the phase-current waveform of the previous method [36], and 10.7 kHz for the square-shape phase-current waveform; that at the rotation speed of 2000 r/min was observed to be 10.8 kHz for the phase-current waveform of the proposed method, 10.5 kHz for the phase-current waveform of the previous method [36], and 9.7 kHz for the square-shape phase-current waveform. Therefore, the switching frequency was far higher than in a normal motor drive application. This experimental setting for the switching frequency deteriorated the efficiency of the experimental motor driving system. However, the reason for this high switching frequency was to accurately generate the phase-current waveforms to be tested, as the scope of this experiment was to evaluate the torque and input-current ripple reduction by the proposed method rather than to achieve the highest efficiency.

The SRM was operated at the output torque of 6 N·m and the rotation speeds of 250 r/min and 2000 r/min. The torque ripple was evaluated only at 250 r/min to avoid the mechanical resonance frequency of the test bench, which occurred at approximately 300 Hz, although the measurement frequency range of the instantaneous torque meter covered up to 6 kHz. The motor test bench of this experiment utilized the leaf spring in the shaft couplings to cope with the misalignment of the shafts. Therefore, the shaft couplings had small torsional stiffness, reducing the torsional resonance frequency of the shaft. This is the reason why 250 r/min was chosen for the measurement of the torque ripple.

The output signal of the instantaneous torque meter contained small fluctuations; these were independent of the electrical angle and therefore could be attributed to the mechanical resonance of the test bench, as well as the load fluctuations. Therefore, the instantaneous torque waveform was determined by measuring the output signal of the instantaneous torque meter 16 times, and then averaging these 16 measured signals.

The three phase-current waveforms to be tested were derived according to the same derivation procedure as described in the previous section. The only difference was that the magnetic co-energy was modeled based on the experimentally measured relation between the phase flux linkage and phase current. For the square-shape phase-current waveform, the firing angle, extinction angle, and peak value were determined as 205 degrees, 360 degrees, and 59 A for 250 r/min, respectively, and 200 degrees, 360 degrees, and 60 A for 2000 r/min, respectively. Finally, the derived phase-current waveforms were stored in the look-up table as shown in Fig. 11. This look-up table contained the data of the phase-current value for every degree of the electrical angle.

Fig. 12 shows the operating waveforms as observed at the rotation speed of 250 r/min. The ripple ratios of the torque and input-current ripples are also presented in Fig. 12(b) and Fig. 12(c), respectively. The torque ripple ratios of the proposed method, previous method [36], and square-shape phase-current are 31%, 51%, and 38%, respectively. The input-current ripple ratios of the proposed method, previous method [36], and square-shape phase-current are 49%, 53%, and 274%, respectively. These experimental results indicate that the proposed method exhibits suppression of both the torque and input-current ripples, consistent with the simulation results.

Fig. 13 shows the operating waveforms as observed at the rotation speed of 2000 r/min. The ripple ratio of the input current ripple is also presented in Fig. 13(b). The input-current ripple ratios of the proposed method, previous method [36], and square-shape phase-current are 63%, 81%, and 158%, respectively. Although the torque ripple cannot be measured at this high rotation speed, the input current ripple is successfully reduced by the proposed method. Consequently, the experiment also supports the reduction of the torque and input-current ripples by the proposed method.

The experimental results exhibit a smaller suppression effect of the input-current ripple than the simulation results particularly in 250 r/min, although the experimental results exhibit a similar suppression effect of the torque ripple. The main reason may lie in the power loss generated in the experimental system. In particular, the input current was derived in the theory while neglecting the power loss at the inverter and motor, whereas the torque was only dependent on the phase current. The proposed method is based on the theoretical analysis of the SRM drive without considering the copper and iron losses of the motor, as well as the switching and conduction losses of the inverter. The simulation of the previous section did not include the power loss, as is the same as with the theory. However, the experimental results may have been significantly affected by the power loss. Particularly, the operation at low rotation speed as 250 r/min has small efficiency, which might have significantly affected the input-current ripple reduction effect by the phase-current waveform of the propose method. Therefore, further reduction of the input-current ripple could be obtained by further including the power loss in the theoretical analysis for deriving the phase-

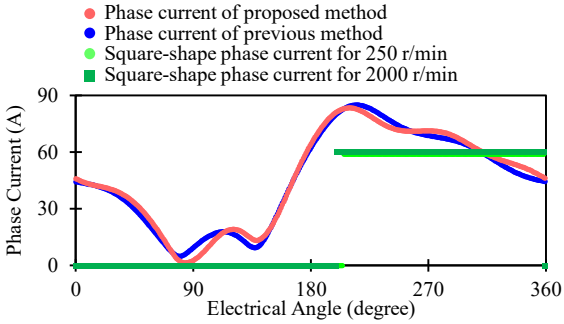

Fig. 11. Phase current command value stored in look-up-table.

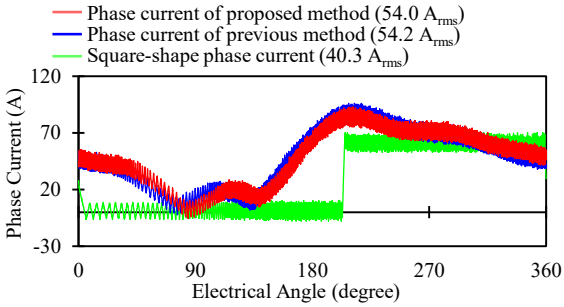

(a) Phase current

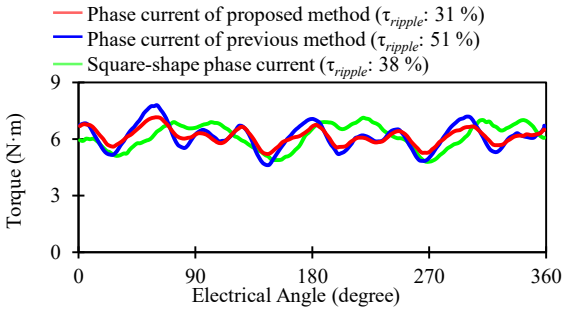

(b) Torque

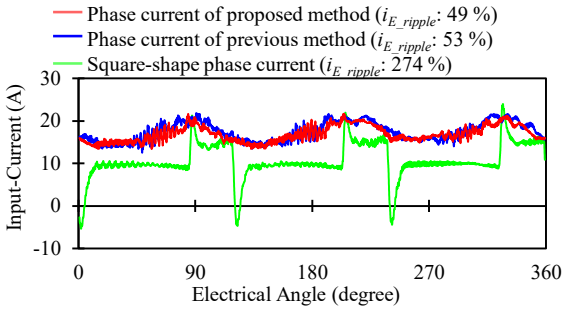

(c) Input current

Fig. 12. Experiment results at 250 r/min.

current waveform.

Meanwhile, because the experiment and simulation exhibited similar torque ripple ratios from the proposed method, the remaining torque ripple in the proposed method may have the same reasons as that in the simulation. These reasons include the limited order of approximation for the nonlinear magnetic model of the motor, limited order for the Fourier expansion to

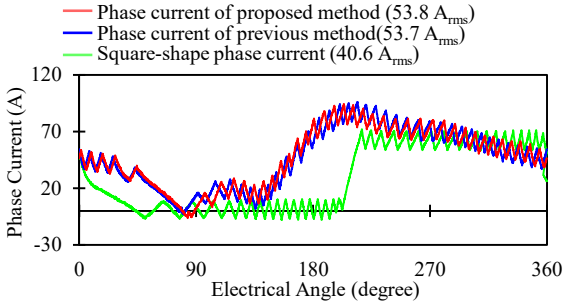

(a) Phase current

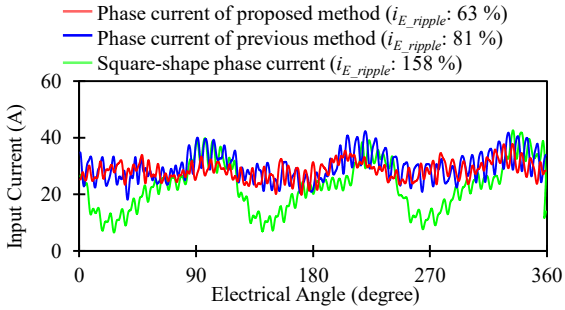

(b) Input current

Fig. 13. Experiment results at 2000 r/min.

determine $g(\theta_E)$ and $k(\theta_E)$ in the derivation process of the phase-current waveform, and the limited repetition of the derivation process for i_{MU}. Therefore, a further torque ripple reduction may be obtained by increasing the order of approximation of the magnetic model as well as $g(\theta_E)$ and $k(\theta_E)$, and by increasing the number of repetitions for the derivation of i_{MU}.

VI. Conclusions

The application of SRMs to vehicular propulsion has been hindered by their comparatively large torque and input-current ripples. A previous study [36] proposed a method for deriving the phase-current waveform that can eliminate both of these ripples. However, this previous method [36] did not consider the magnetic nonlinearity of the magnetic saturation. Consequently, the elimination of these ripples greatly deteriorated at high torque output, and the magnetic saturation significantly affected the torque and the input current.

This study addresses this issue by proposing an improved method that further incorporates the effects of the magnetic saturation on the torque and input-current ripples. The proposed method is based on a nonlinear magnetic model considering the magnetic saturation. Therefore, the proposed method can derive the phase-current waveform for reducing the torque and input-current ripples for various operating conditions, including in high-output-torque operation, in which the magnetic saturation cannot be neglected. The experiment and simulation verify the reductions in both the torque and input-current ripples, supporting the effectiveness of the proposed method.

Nonetheless, the experimental results exhibit a smaller reduction effect on the input-current ripple than the simulation. This discrepancy may be attributed to the power loss at the motor and the inverter, which were not considered in the theory,

as well as in the simulation. This implies that a further input-current ripple reduction can be obtained by developing the phase-current waveform derivation method based on a motor driving model incorporating both the nonlinear magnetic property and power loss, which should be ad dressed in future research.

Furthermore, the experimental results, as well as the simulation results, still contain approximately 30% of the torque ripple. This remaining torque ripple may be attributed by the insufficient optimization of the phase-current waveform by the proposed method. Therefore, a further torque ripple reduction can be obtained by improving the calculation method according to the proposed method; this should also be addressed in future research.

REFERENCES

[1] Z. Q. Zhu and C. C. Chan, "Electrical machine topologies and technologies for electric, hybrid, and fuel cell vehicles," in *Proc. IEEE Vehicle Power Propulsion Conf.*, Harbin, China, pp. 1–6, Sept. 2008.

[2] W. Suppharangsan and J. Wang, "Experimental validation of a new switching technique for DC-link capacitor minimization in switched reluctance machine drives," in *Proc. IEEE Int. Electric Machines Drives Conf.*, Chicago, USA, pp. 1031–1036, May 2013.

[3] I. Husain and M. Ehsani, "Torque ripple minimization in switched reluctance motor drives by PWM current control," *IEEE Trans. Power Electron.*, vol. 11, no. 1, pp. 83-88, Jan. 1996.

[4] T. Kusumi, T. Hara, K. Umetani, and E. Hiraki, "Theoretical Derivation of Phase Current Profile for Switched Reluctance Motors to Suppress Radial Force Ripple and Torque Ripple," in *Proc. IEEE Intl Symposium Ind. Electron.*, Cairns, QLD, Australia, pp. 1037–1042 June 2018.

[5] M. Kawa, K. Kiyota, J. Furqani, and A. Chiba, "Acoustic noise reduction of a high-efficiency switched reluctance motor for hybrid electric vehicles with novel current waveform," *IEEE Trans. Ind. Appl.*, vol. 55, no. 3, pp. 2519-2528, May 2019.

[6] J. W. Lee, H. S. Kim, B. I. Kwon, and B. T. Kim, "New rotor shape design for minimum torque ripple of SRM using FEM," *IEEE Trans. Magn.*, vol. 40, no. 2, pp. 754-757, Mar. 2004.

[7] N. K. Sheth and K. R. Rajagopal, "Torque profiles of a switched reluctance motor having special pole face shapes and asymmetric stator poles," *IEEE Trans. Magn.*, vol. 40, no. 4, pp. 2035-2037, Jul. 2004.

[8] Y. K. Choi, H. S. Yoon, and C. S. Koh, "Pole-shape optimization of a switched-reluctance motor for torque ripple reduction," *IEEE Trans. Magn.*, vol. 43, no. 4, pp. 1797-1800, Apr. 2007.

[9] M. Rodrigues, P. J. Costa Branco, and W. Suemitsu, "Fuzzy logic torque ripple reduction by turn-off angle compensation for switched reluctance motors," *IEEE Trans. Ind. Electron.*, vol. 48, no. 3, pp. 711-715, June 2001.

[10] I. Husain, "Minimization of torque ripple in SRM drives," *IEEE Trans. Ind. Electron.*, vol. 49, no. 1, pp. 28-39, Feb. 2002.

[11] L. O. A. P. Henriques, P. J. Costa Branco, L. G. B. Rolim, and W. I. Suemitsu, "Proposition of an offline learning current modulation for torque-ripple reduction in switched reluctance motors: design and experimental evaluation," *IEEE Trans. Ind. Electron.*, vol. 49, no. 3, pp. 665-676, June 2002.

[12] A. D. Cheok and Y. Fukuda, "A new torque and flux control method for switched reluctance motor drives," *IEEE Trans. Power Electron.*, vol. 17, no. 4, pp. 543-557, Jul. 2002.

[13] P. L. Chapman and S. D. Sudhoff, "Design and precise realization of optimized current waveforms for an 8/6 switched reluctance drive," *IEEE Trans. Power Electron.*, vol. 17, no. 1, pp. 76-83, Jan. 2002.

[14] C. Mademlis and I. Kioskeridis, "Performance optimization in switched reluctance motor drives with online commutation angle control," *IEEE Trans. Energy Convers.*, vol. 18, no. 3, pp. 448-457, Sept. 2003.

[15] A. M. Omekanda, "A new technique for multidimensional performance optimization of switched reluctance motors for vehicle propulsion," *IEEE Trans. Ind. Appl.*, vol. 39, no. 3, pp. 672-676, May 2003.

[16] N. T. Shaked and R. Rabinovici, "New procedures for minimizing the torque ripple in switched reluctance motors by optimizing the phase-current profile," *IEEE Trans. Magn.*, vol. 41, no. 3, pp. 1184-1192, Mar. 2005.

[17] X. D. Xue, K. W. E. Cheng, and S. L. Ho, "Optimization and evaluation of torque-sharing functions for torque ripple minimization in switched reluctance motor drives," *IEEE Trans. Power Electron.*, vol. 24, no. 9, pp. 2076-2090, Sept. 2009.

[18] D. H. Lee, J. Liang, Z. G. Lee, and J. W. Ahn, "A simple nonlinear logical torque sharing function for low-torque ripple SR drive," *IEEE Trans. Ind. Electron.*, vol. 56, no. 8, pp. 3021 – 3028, Aug. 2009.

[19] X. D. Xue, K. W. E. Cheng, J. K. Lin, Z. Zhang, K. F. Luk, T. W. Ng, and N. C. Cheung, "Optimal control method of motoring operation for srm drives in electric vehicles," *IEEE Trans. Veh. Technol.*, vol. 59, no. 3, pp. 1191-1204, Mar. 2010.

[20] V. P. Vujičić, "Minimization of torque ripple and copper losses in switched reluctance drive," *IEEE Trans. Power Electron.*, vol. 27, no. 8, pp. 388-399, Jan. 2012.

[21] C. Moron, A. Garcia, E. Tremps, and J. A. Somolinos, "Torque control of switched reluctance motors," *IEEE Trans. Magn.*, vol. 48, no. 4, pp. 1661-1664, Apr. 2012.

[22] R. Mikail, I. Husain, Y. Sozer, M. S. Islam, and T. Sebastian, "Torque-ripple minimization of switched reluctance machines through current profiling," *IEEE Trans. Ind. Appl.*, vol. 49, no. 3, pp. 1258-1267, May 2013.

[23] J. Ye, B. Bilgin, and A. Emadi, "An offline torque sharing function for torque ripple reduction in switched reluctance motor drives," *IEEE Trans. Energy Convers.*, vol. 30, no. 2, pp. 726-735, June 2015.

[24] J. Ye, B. Bilgin, and A. Emadi, "An extended-speed low-ripple torque control of switched reluctance motor drives," *IEEE Trans. Power Electron.*, vol. 30, no. 3, pp. 1457-1470, Mar. 2015.

[25] P. Dúbravka, P. Rafajdus, P. Makyš, and L. Szabó, "Control of switched reluctance motor by current profiling under normal and open phase operating condition," *IET Electric Power Appl.*, vol. 11, no. 4, pp. 548-556, Apr. 2017.

[26] H. Li, B. Bilgin, and A. Emadi, "An improved torque sharing function for torque ripple reduction in switched reluctance machines," *IEEE Trans. Power Electron.*, vol. 34, no. 2, pp. 1635-1644, Feb. 2019.

[27] T. Husain, A. Elrayyah, Y. Sozer, and I. Husain, "Unified control for switched reluctance motors for wide speed operation," *IEEE Trans. Ind. Electron.*, vol. 66, no. 5, pp. 3401-3411, May 2019.

[28] N. K. Sheth and K. R. Rajagopal, "Optimum pole arcs for a switched reluctance motor for higher torque with reduced ripple," *IEEE Trans. Magn.*, vol. 39, no. 5, pp. 3214-3216, Sept. 2003.

[29] G. Li, J. Ojeda, S. Hlioui, E. Hoang, M. Lecrivain, and M. Gabsi, "Modification in rotor pole geometry of mutually coupled switched reluctance machine for torque ripple mitigating," *IEEE Trans. Magn.*, vol. 48, no. 6, pp. 2025-2034, June 2012.

[30] B. Anvari, H. A. Toliyat, and B. Fahimi, "Simultaneous optimization of geometry and firing angles for in-wheel switched reluctance motor drive," *IEEE Trans. Transport. Electrific.*, vol. 4, no. 1, pp. 322-329, Mar. 2018.

[31] C. R. Neuhaus, N. H. Fuengwarodsakul, and R. W. De Doncker, "Control scheme for switched reluctance drives with minimized DC-link capacitance," *IEEE Trans. Power Electron.*, vo l. 23, no. 5, pp. 2557-2564, Sept. 2008.

[32] W. Suppharangsan, and J. Wang, "Switching technique for minimisation of DC-link capacitance in switched reluctance machine drives," *IET Elect. Syst. Transportation*, vol. 5, no. 4, pp. 185-193, Dec. 2015.

[33] F. Yi and W. Cai, "A quasi-Z-source integrated multiport power converter as switched reluctance motor drives for capacitance reduction and wide-speed-range operation," *IEEE Trans. Power Electron.*, vol. 31, no. 11, pp. 7661-7676, Nov. 2016.

[34] W. Cai and F. Yi, "An integrated multiport power converter with small capacitance requirement for switched reluctance motor drive," *IEEE Trans. Power Electron.*, vol. 31, no. 4, pp. 3016-3026, Apr. 2016.

[35] F. Yi and W. Cai, "Modeling, control, and seamless transition of the bidirectional battery-driven switched reluctance motor/generator drive based on integrated multiport power converter for electric vehicle," *IEEE Trans. Power Electron.*, vol. 31, no. 10, pp. 7099-7111, Oct. 2016.

[36] T. Kusumi, T. Hara, K. Umetani, and E. Hiraki, "Phase-current waveform for switched reluctance motors to eliminate input-current ripple and torque ripple in low-power propulsion below magnetic saturation," *IET Power Electron.*, vol. 13, no. 15, pp. 3351–3359, Nov. 2020.

[37] T. Kusumi, T. Hara, K. Umetani, and E. Hiraki, “Simultaneous Tuning of Rotor Shape and Phase Current of Switched Reluctance Motors for Eliminating Input Current and Torque Ripples with Reduced Copper Loss,” *IEEE Trans. Ind. Appl.*, vol. 56, no. 6, pp. 6384–6398, Nov.-Dec. 2020.
[38] T. Kusumi, K. Kobayashi, K. Umetani, and E. Hiraki, “Analytical Derivation of Phase Current Waveform Eliminating Torque Ripple and Input Current Ripple of Switched Reluctance Motors under Magnetically Saturated Operation,” in *Proc. IEEE Energy Conversion Congr. Expo. (ECCE2019)*, Baltimore, MD, USA, pp. 6540-6547, Oct. 2019.
[39] T. Hara, T. Kusumi, K. Umetani, and E. Hiraki, “A simple behavior model for switched reluctance motors based on magnetic energy,” in *Proc. Intl. Power Electron. Motion Ctrl. Conf. (IPEMC2016)*, Hefei, China, May. 2016.
[40] D. N. Essah and S. D. Sudhoff, “An improved analytical model for the switched reluctance motor,” *IEEE Trans. Energy Convers.*, vol. 18, no. 3, pp. 349-356, Sept. 2003.
[41] J. Furqani, M. Kawa, K. Kiyota, and A. Chiba, “Current Waveform for Noise Reduction of a Switched Reluctance Motor Under Magnetically Saturated Condition,” *IEEE Trans. Ind. Appl.*, vol. 54, no. 1, pp. 213–222, Jan.-Feb. 2018.

Takayuki Kusumi (Member, IEEE) was born in Okayama, Japan. He received the M.S. and Ph.D. degrees in electrical engineering from Okayama University, Okayama, Japan, in 2017 and 2021, respectively.

He is currently with Mazda Motor Corporation, Hiroshima, Japan. His research interest includes control technique for electrical machines for vehicular applications.

Kosuke Kobayashi was born in Shizuoka, Japan. He received the B.S. and M.S. degrees in electrical engineering from Okayama University, Okayama, Japan, in 2019 and 2021, respectively.

He is currently with Honda R&D Co., Ltd., Saitama, Japan. His research interest includes control technique of switched reluctance motors and power magnetics for industrial applications.

Kazuhiro Umetani (Member, IEEE) was born in Kobe, Japan. He received the M.S. and Ph.D. degrees in geophysical fluid dynamics from Kyoto University, Kyoto, Japan, in 2004 and 2007, respectively, and the second Ph.D. degree in electrical engineering from Shimane University, Matsue, Japan, in 2015.

From 2007 to 2008, he was a Circuit Design Engineer for Toshiba Corporation, Tokyo, Japan. From 2008 to 2014, he was with the Power Electronics Group, DENSO CORPORATION, Kariya, Japan. From 2014 to 2020, he was an Assistant Professor with the Okayama University, Okayama, Japan. From 2020 to 2021, he was an Associate Professor with the Tohoku University, Miyagi, Japan. He is currently an Associate Professor with the Okayama University, Okayama, Japan. His research interests include new circuit configurations in power electronics and power magnetics for vehicular applications.

Dr. Umetani is a Member of the Institute of Electrical Engineers of Japan and the Japan Institute of Power Electronics.

Eiji Hiraki (Member, IEEE) was born in Yamaguchi, Japan. He received the M.Sc. and Ph.D. degrees in electrical engineering from Osaka University, Osaka, Japan, in 1990 and 2004, respectively.

He joined Mazda Motor Corporation, Hiroshima, Japan, in 1990. From 1995 to 2013, he was with the Power Electronics Laboratory, Yamaguchi University, Yamaguchi, Japan. He is currently a Professor with the Electric Power Conversion System Engineering Laboratory, Okayama University, Okayama, Japan. His research interests include circuits and control systems of power electronics, particularly soft-switching technique for high-frequency switching power conversion systems.

Dr. Hiraki is a Member of the Institute of Electrical Engineers of Japan and the Japan Institute of Power Electronics.